Materials Today Bio 16 (2022) 100362

Contents lists available at ScienceDirect

Materials Today Bio

journal homepage: www.journals.elsevier.com/materials-today-bio

$SrFe_{12}O_{19}$-doped nano-layered double hydroxide/chitosan layered scaffolds with a nacre-mimetic architecture guide in situ bone ingrowth and regulate bone homeostasis

Yu-Wei Ge [a,1], Zhang-Hao Fan [b,1], Qin-Fei Ke [b], Ya-Ping Guo [b,***], Chang-Qing Zhang [a,**], Wei-Tao Jia [a,*]

[a] Department of Orthopedic Surgery, Shanghai Jiao Tong University Affiliated Sixth People's Hospital, Shanghai, 200233, People's Republic of China
[b] The Education Ministry Key Lab of Resource Chemistry and Shanghai Key Laboratory of Rare Earth Functional Materials, Shanghai Normal University, Shanghai, 200234, China

ARTICLE INFO

Keywords:
Bone regeneration
Bone homeostasis
Inflammatory
Nacre-mimetic
Layered double hydroxides

ABSTRACT

Osteoporotic bone defects result from an imbalance in bone homeostasis, excessive osteoclast activity, and the weakening of osteogenic mineralization, resulting in impaired bone regeneration. Herein, inspired by the hierarchical structures of mollusk nacre, nacre exhibits outstanding high-strength mechanical properties, which are in part due to its delicate layered structure. $SrFe_{12}O_{19}$ nanoparticles and nano-layered double hydroxide (LDH) were incorporated into a bioactive chitosan (CS) matrix to form multifunctional layered nano-$SrFe_{12}O_{19}$-LDH/CS scaffolds. The compressive stress value of the internal ordered layer structure matches the trabecular bone (0.18 MPa). The as-released Mg^{2+} ions from the nano-LDH can inhibit bone resorption in osteoclasts by inhibiting the NFκB signaling pathway. At the same time, the as-released Sr^{2+} ions promote the high expression of osteoblast collagen 1 proteins and accelerate bone mineralization by activating the BMP-2/SMAD signaling pathway. *In vivo,* the Mg^{2+} ions released from the $SrFe_{12}O_{19}$-LDH/CS scaffolds inhibited the release of pro-inflammatory factors (IL-1β and TNF-α), while the as-released Sr^{2+} ions promoted osteoblastic proliferation and the mineralization of osteoblasts inside the layered $SrFe_{12}O_{19}$-LDH/CS scaffolds. Immunofluorescence for OPG, RANKL, and CD31, showed that stable vasculature could be formed inside the layered $SrFe_{12}O_{19}$-LDH/CS scaffolds. Hence, this study on multifunctional $SrFe_{12}O_{19}$-LDH/CS scaffolds clarifies the regulatory mechanism of osteoporotic bone regeneration and is expected to provide a theoretical basis for the research, development, and clinical application of this scaffold on osteoporotic bone defects.

1. Introduction

Bone defect regeneration and repair (such as trauma [1], tumor removal [2], infection [3] and periprosthetic osteolysis [4]) have always been a challenging yet important issue in the field of orthopedics. The aging of bone marrow mesenchymal stem cells, the decrease in bone mineralization ability, and excessive osteoclast activity cause severe loss of bone mass, especially in patients with osteoporosis [5,6]. This results in an imbalance in bone homeostasis, so the regeneration and repair of bone defects become even more important [7]. At present, preferred criteria for clinical treatment of bone defects caused by the above factors is autologous bone transplantation; however, the source and size of autologous bone are limited, making it difficult to meet clinical needs [3,8]. Autologous bone transplantation is scarce, especially for patients with osteoporotic bone defects. At present, various artificial bone materials created from tissue engineering have problems such as insufficient mechanical strength, easy to cause acute inflammatory response [9,10], promote osteoclast differentiation [11], form fibrous encapsulations, and

*** Corresponding author.
** Corresponding author.
* Corresponding author. Department of Orthopedic Surgery, Shanghai Jiao Tong University Affiliated Sixth People's Hospital, Shanghai, 200233, People's Republic of China.
E-mail addresses: ypguo@shnu.edu.cn (Y.-P. Guo), zhangcq@sjtu.edu.cn (C.-Q. Zhang), jiaweitao@shsmu.edu.cn (W.-T. Jia).
[1] These authors contributed equally to this work.

https://doi.org/10.1016/j.mtbio.2022.100362
Received 2 May 2022; Received in revised form 20 June 2022; Accepted 9 July 2022
Available online 19 July 2022

promote bone resorption, significantly reducing the performance of the implanted material.

Most of the current research focuses on changing the morphology and structure of bio-scaffolds, or applying modification techniques such as surface modification chemical bonds to achieve the ability to promote bone regeneration [12–14]. Especially in recent years, a lot of studies have focused on building various material delivery tools to load pro-osteogenic or osteoclast-inhibiting drugs, and targeted therapy through local application or intravenous injection [15,16]. But for patients with osteoporosis, due to the imbalance of osteogenic mineralization and osteoclast bone resorption, and the synergistic imbalance of osteogenesis is purely through the transient release of pro-osteogenic or osteoclast-inhibiting drugs, without starting from the source of its pathophysiology, ignoring the management of the local immune microenvironment, and failing to fully consider the two aspects of osteogenesis and osteoclasts. Therefore, it is difficult to achieve the purpose of clinical treatment.

Layered double hydroxides (LDHs) have been reported as drug delivery system and antibacterial platforms, owing to their good biocompatibility and positive charge [17–19]. The LDH material is rich in Mg^{2+} ions, which are indispensable in the regulation of bone homeostasis. Magnesium ions promote bone regeneration by activating osteoblast differentiation and adhesion. In addition, Mg^{2+} plays a critical role in inhibiting the RANKL-mediated differentiation of macrophages into osteoclasts [20,21]. Studies have shown that Mg^{2+} also inhibits the differentiation and maturation of osteoclast cells by inhibiting three common osteoclast pathways: NF-κB, ERK, and AKT [22–24]. Therefore, Mg metal implants and their derivatives have been used clinically. However, magnesium metal implants also have many shortcomings, such as the mismatch between the material degradation and the bone formation, the generation of a large amount of hydrogen, and the formation of a magnesium oxide coating on the implant surface [25–27].

Static magnetic fields (SMFs) are proved as a noval physical stimulus strategy to induce cellar proliferation and osteogenic differentiation [28,29]. During the process of bone regeneration and reconstruction, the SMFs could activate the NF-κB, integrin, MAPK and BMP-2/Smad pathways [29,30]. Upon to now, magnetic Fe_3O_4 nanoparticles have been incorporated in bone scaffolds for the enhanced cell viability and bone regeneration [31,32]. However, Fe_3O_4 nanoparticles lack strong magnetic properties because of their superparamagnetic feature. To overcome this disadvantage, M-type $SrFe_{12}O_{19}$ ferrite becomes an alternative magnetic materials because of its great saturation magnetization and coercivity [30]. The incorporation of $SrFe_{12}O_{19}$ nanoparticles in bone scaffolds plays an important role in recruiting endogenous stem cells and facilitating bone regeneration [30,33]. The metal cations derived from the degradation of $SrFe_{12}O_{19}$ nanoparticles are composed of Sr^{2+} and Fe^{3+} ions. Previous works have confirmed that Fe_3O_4 nanoparticles showed excellent biocompatibilitly and bioactivity without obvious toxicity to stem cells and bone tissues [31,32]. In addition, the degradation product of Sr^{2+} ions could act as an activator of bone mineralization and is an inhibitor of bone resorption [34–37]. Sr^{2+} ions can maintain bone homeostasis [38,39]. It has been reported that Sr^{2+} can promote early endochondral osteogenesis and mineralization of bone [40]. The similarity in size and polarity between Sr^{2+} ions and Ca^{2+} ions facilitates the ion exchange between Sr^{2+} and Ca^{2+} in bone tissue [41]. Simultaneously, Sr^{2+} can promote angiogenesis and achieve bone repair [40,42,43]. Recently, some researchers have also reported that Sr can inhibit macrophage polarization [44,45], inhibit the release of IL-1β and TNF-α factors, and inhibit the formation of fibrous tissue [46,47].

Inspired by the brick-and-mortar structures of nacre in nature, the layers are interconnected by a biopolymer matrix [48,49]. In this experiment, nano-$SrFe_{12}O_{19}$ and nano-LDH were deposited on the surface of chitosan to prepare a multi-layer structure to enhance its biological strength. And the characteristics of Sr and Mg jointly involved in regulating bone homeostasis were used to treat a clinical osteoporotic bone defect disease model. The root cause of the difficulty in repairing osteoporotic bone defects is the imbalance in bone homeostasis and the synergistic effect of osteogenesis and osteoclast destruction, which is manifested as the enhanced bone resorption of osteoclasts and weakened bone mineralization ability of osteoblasts. To overcome these problems, we first constructed a multifunctional nano-$SrFe_{12}O_{19}$-LDH/CS scaffold that can inhibit the hyperactive state of osteoclasts, which could reduce the pro-inflammatory factors. And then the fabricated multifunctional layered nano-$SrFe_{12}O_{19}$-LDH/CS scaffold regulated the mineralization of osteoblasts, restored the normal synergistic effect between osteogenesis and osteoclast activity, and reversed local bone homeostasis imbalance to promote bone ingrowth and regeneration.

2. Methods

2.1. Preparation of LDH powder

The nano-LDH powders were fabricated via chemical precipitation. $Mg(NO_3)_2{\cdot}6H_2O$ and $Al(NO_3)_3{\cdot}9H_2O$ (Mg/Al molar ratio of 3.0) were added into the ddH_2O to get a salt solution. And an alkali solution was prepared by adding NaOH into deionized water. Then the salt and alkali solutions were simultaneously dropped into a three-necked flask with deionized water (150 ml) at 40 °C under constant stirring. The PH value of the mixture was maintained to be 10–11. Finally, the LDH products were washed with deionized water, collected by filtration, and dried at 60 °C for 48 h.

2.2. Preparation of $SrFe_{12}O_{19}$-LDH/CS scaffold

CS powder (2.0 g) and magnetic $SrFe_{12}O_{19}$ nanoparticles (0.2 g) were added to the acetic acid solution (2.0 vol%, 50 ml). This process has been stirred for 3 h. Subsequently, the LDH powder (2.0 g) prepared above was added to the CS solution and stirred continuously for 2 h. After stirring for 2 h and ultrasounding for 30 min, then the mixture were transferred into 24-well plates or 96-well plates. The above samples were quickly transferred to −80 refrigerator and frozen for more than 5 h. The above samples were freeze-dried in a freeze-dryer at −60 °C for 48 h. The samples were then soaked in 5 wt% NaOH for 24 h and washed with ddH_2O for 4 days. The $SrFe_{12}O_{19}$-LDH/CS scaffolds were prepared after freezing-dried again. The weight percentages of $SrFe_{12}O_{19}$, LDH and CS were 4.76%, 47.62% and 47.62%, respectively. In addition, the LDH/CS scaffolds as a control group were prepared under the same conditions without adding magnetic powders.

2.3. Characterization

The phase structures of the CS, $SrFe_{12}O_{19}$, LDH powder, and $SrFe_{12}O_{19}$-LDH/CS scaffolds were characterized via X-ray powder diffraction (XRD, D/MAX-111C, Japan). And fourier transform infrared spectroscopy (FTIR; Frontier, PerkinElmer, USA) at a voltage of 100–230 V in the wavenumber range 4000–500 cm^{-1} was used to detect the functional groups. The morphologies were investigated using scanning electron microscopy (SEM; JSM-6380LV) with energy-dispersive spectrometry (EDS). A vibrating sample magnetometer (VSM, YP Magnetic Technology Development Co., LTD, Jilin, China) was used to detect the hysteresis loops of $SrFe_{12}O_{19}$ nanoplates and $SrFe_{12}O_{19}$-LDH/CS scaffolds. The compressive strengths of the LDH/CS and $SrFe_{12}O_{19}$-LDH/CS scaffolds ($r = 0.75$ cm, $h = 1.5$ cm) were tested using a microcomputer-controlled electronic universal testing machine (WDW-0.5C, Shanghai Hualong Microelectronics Co. Ltd., China) at a compression speed of 5 mm/min. For *in vitro* degradation assays, the $SrFe_{12}O_{19}$-LDH/CS scaffolds were cut into small pieces. 0.4 g $SrFe_{12}O_{19}$-LDH/CS scaffolds were soaked in a centrifuge tube with 9.0 ml deionized water. At different time points (12 h, 24 h, 48 h, 72 h, 96 h, 120 h, 144 h), 5 ml immersion solution was extract, and the corresponding ion concentrations were detected by an inductively coupled plasma/optical emission spectrometry (ICP; iCAP 7000, Thermo Fisher, USA). In addition, 5 ml fresh

immersion medium was added again to keep the same volume during the whole release process.

2.4. Cell culture, toxicity and adhesion

Bone marrow macrophages (BMM) and MC-3T3-E1 were cultured as previously reported [50,51]. Eight-week-old c57BL/6 mice were sacrificed by cervical dislocation. Soak them in 75% alcohol for 20 min. Then use sterile ophthalmic scissors and forceps to separate and remove the muscle and fascia, and take out the tibia, fibula and femur. Finally, we cultured BMMs in medium containing recombinant M-CSF protein (30 ng/ml). They were considered for use when the BMM cell density was approximately 80%. In the osteoclast induction differentiation experiment, we chose the medium containing M-CSF(30 ng/ml) and Rankl(50 ng/ml) to continue to culture macrophages. The extracts were prepared according to the ISO 10993–5. The ratio of mass to extraction medium was 0.2 g/mL, and the immersed samples were kept in a humidified atmosphere with 5% CO2 at 37 °C for 24 h. After 24 h, the above-mentioned extraction solution was taken out and placed in a 4° refrigerator for subsequent use, and an equal amount of the above-mentioned volume of culture medium was added to soak the samples. For the cell toxicity test, we chose the cell counting kit-8 (CCK-8; Dojindo, Kumamoto, Japan). The medium was changed to extraction solutions for the LDH/CS and $SrFe_{12}O_{19}$-LDH/CS scaffolds. MC-3T3-E1 cells were seeded at a density of 10^4 in 96-well plates for 1, 2, 3 and 4 days, respectively. After that, the culture environment was changed to the above-mentioned extraction of scaffold (100μl/well). Finally, according to the instructions of CCK-8 reagent, the reagent was added and the incubation was continued for 1 h. Then the samples were tested for absorbance on the machine (OD value was set at 450/630). We place sterile scaffolds (LDH/CS and $SrFe_{12}O_{19}$-LDH/CS scaffolds) in a 24-well plate in advance. Three replicates were prepared for each group of samples. The hBMSCs (10^4/per well) were seeded on the surface of the scaffold to examine cell adhesion. Then, the scaffolds were dehydrated in a graded manner. The above samples were freeze-dried again. Finally, the morphology of the hBMSCs on the scaffolds was characterized using SEM (Sirion 200, FEI, Hillsboro, OR, USA).

2.5. ALP and alizarin red

MC3T3-E1 cells were seeded in 24-well plates at a density of 5×10^4. After that, we use 1 ml of conditioned medium per well (extraction of the LDH/CS scaffolds and $SrFe_{12}O_{19}$-LDH/CS scaffolds). Control, LDH/CS, and $SrFe_{12}O_{19}$-LDH/CS groups were prepared, and the cells were further cultured for 7 and 21 d. After that, the cells were fixed with 4% paraformaldehyde. Then the samples were washed three times with PBS for 10 min each time. Finally, the samples were stained using an ALP kit (Hongqiao, Shanghai, China) and an Alizarin Red staining kit (Sigma-Aldrich, Darmstadt, Germany) according to the reagent manufacturer's instructions.

2.6. TRAP and F-actin staining

Bone marrow macrophages (BMMs) were seeded in a 96-well plate at a density of 10^4. After that, we use 100 μl of conditioned medium containing 30 ng/ml MCSF and 50 ng/ml RANKL protein (extraction of the LDH/CS scaffolds and $SrFe_{12}O_{19}$-LDH/CS scaffolds). Control, LDH/CS, and $SrFe_{12}O_{19}$-LDH/CS groups were prepared. The BMMs were cultured for 7 days, and the medium was changed every 2 days. Afterward, the BMM cells were fixed with 4% paraformaldehyde. Then the samples were washed three times with PBS for 10 min each time. Finally, the cells were stained using a TRAP kit (Sigma-Aldrich) and rhodamine-conjugated phalloidin (Cytoskeleton Inc., Denver, CO, USA). Finally, the TRAP staining were observed under a light microscope. Cells with >3 nuclei indicate TRAP positivity. The cytoskeleton was visualized using an LSM5 confocal microscope.

2.7. RT-qPCR and WB

MC3T3-E1 cells were seeded in a 6-well plate at a density of 4×10^5 for 24 h and grouped into Control, LDH/CS, and $SrFe_{12}O_{19}$-LDH/CS groups. After that, the extraction solution of the scaffold material was changed every 2 days. The above samples were further cultured for 7 days. Total RNA was extracted using the EZ-press RNA Purification Kit. SYBR Green qPCR Master Mix and ABI 7500 Sequencing Detection System (Applied Biosystems; Thermo Fisher Scientific, Inc.) were used to perform qPCR. The PCR primers were designed to amplify the genes of interest are shown Table 1.

To verify osteoblast differentiation protein expression, MC3T3-E1 cells were seeded in a 6-well plate at a density of 4×10^5 for 24 h. After that, the extraction solution of the scaffold material was changed every 2 days. The expression of osteoblast-associated proteins Bmp-2, Runx-2, Col-1, and P-Smad1/5 was measured. To verify the expression of osteoclast differentiation proteins, BMMs were seeded in a 6-well plate at a density of 10^4 for 24 h. After that, the extraction solution of the scaffold material was changed every 2 days. The expression of osteoclast-associated proteins NFATc1, C-fos, Cath-K, *p*-IKBα and *p*-NFκB proteins was measured. All the above samples were cultured for 7 days. Then 200 μl of radioimmunoprecipitation assay (RIPA) lysis buffer (1 μM phosphatase inhibitor; Sangon Biotech Co., Ltd.) was added and centrifuged at a speed of 12,000 rpm for 15 min. After centrifugation, the pellet was removed, and the protein concentration was detected by the bicinchoninic acid assay(BCA). The samples were subjected to SDS-PAGE. Then electrophoresis, transfer membrane, and incubate with primary antibody at 37 °C. An Odyssey infrared imaging system was used to detect protein expression.

2.8. Animal model, microCT and histological evaluation

All procedures were approved by the Animal Ethical of the Shanghai Jiao Tong University Affiliated Sixth People's Hospital (approval number: SYXK2011-0128). Twelve female Sprague-Dawley rats, weighing an average of 200–250 g, were used as bilateral critical-size calvarial defect models to assess bone regeneration. The parameters for bilateral skull defects were set to be 5 mm in diameter and 2 mm in thickness. LDH/CS (n = 4) and $SrFe_{12}O_{19}$-LDH/CS scaffolds (n = 4) were used to fill the defect sites, the periosteum was removed, and the scalp of the rats were sutured. The rats were then injected intraperitoneally with fluorescently labeled alizarin red (30 mg/kg, Sigma-Aldrich) and calcein (30 mg/kg, Sigma-Aldrich) at 3, 21 days before euthanasia, respectively [50]. All rats were euthanized after 12 weeks. The operators then removed the bone defect at the top of the skulls and placed them in 4% paraformaldehyde for 7 days. Finally, the bone defects were investigated using a micro-CT system (Skyscan 1076). Bone mineral density (BMD) and new bone volume/tissue volume (BV/TV) ratios were calculated using appropriate analysis software. After that, a part of the sample was fixed with PMMA, cut with a hard tissue microtome, and the fluorescence was observed via confocal microscopy. The distance between alizarin red and calcein indicates the growth of new bone tissue. Another part of the sample was placed in an EDTA decalcification solution and subjected to immunohistochemistry and fluorescence analysis.

Table 1
PCR primers were designed to amplify the genes of interest are shown below.

GAPDH,	F:5′- CACCACCATGGAGAAGGCCG-3',
RUNX-2,	R:'- ATGATGTTCTGGGCAGCCCC-3'; F:5′- TCGGAGAGGTAC CAGATGGG-3';
COL-1,	R: 5′- TGAAAC TCTTGC CTC GTC CG-3'; F:5′-GAGAGGTGAACAAGGTCC CG 3';
BMP-2,	R:5′- AAA CCT CTC TCG CCT CTTGC -3'; F: 5′- GGAACGGACATTCGGTCCTT -3′; R:5′- CACCATGGTCGACCTTTAGGA -3

2.9. Statistical analysis

The results were presented as the mean ± standard deviation (SD). Comparisons between groups were analyzed using one-way analysis of variance (ANOVA). Statistical analyses were performed using GraphPad Prism 6 software (CA, USA), $^{**}P < 0.01$ and $^{*}P < 0.05$.

3. Results

3.1. Structure and morphology of $SrFe_{12}O_{19}$-LDH/CS scaffold

The phase structure and functional groups present in the $SrFe_{12}O_{19}$ nanoparticles and $SrFe_{12}O_{19}$-LDH/CS scaffolds were observed by XRD and FTIR spectroscopy (Fig. 1). CS is a semicrystalline material; therefore, the characteristic peak of pure CS was located at $2\theta = 20°$. The (003) and (006) planes of LDH represent a double-layered structure (JCPDS No. 14–0191), which depends on the spacing between the adjacent bimetallic hydroxide layers in the LDH lattice. The XRD pattern of $SrFe_{12}O_{19}$ nanoparticles indicated that the characteristic peaks corresponded well to hexagonal phase (JCPDS 80–1157). The characteristic peaks of LDH and M-type ferrite were still detected in the $SrFe_{12}O_{19}$ -LDH/CS composite scaffold (Fig. 1a), indicating that the layered structure was not destroyed. Clear peaks of the (110) and (113) planes were still present, showing good long-range order in the a and b directions of the layered structure.

Fig. 1b–d showed the FTIR spectra of the CS powders, LDH nanoplates and $SrFe_{12}O_{19}$-LDH/CS scaffolds. For the CS powders (Fig. 1b), the –OH or $–NH_2$ stretching vibration and amide-I vibration peaks located at 3506 cm^{-1} and 1661 cm^{-1}, respectively [30,33]. The N–H deformation vibration and wagging vibration peaks located at 1593 cm^{-1} and 895 cm^{-1}, respectively. The C–N characteristic peaks in the primary and secondary amide groups located at 1423/1379 cm^{-1} and 1315/1252 cm^{-1}, respectively [30,33]. The C–O stretching vibration and bridge oxygen stretching vibration peaks located at 1061/1030 cm^{-1} and 1154 cm^{-1}, respectively [30,33]. The peak at 661 cm^{-1} corresponded to the OCO(δ) vibration due to the residual CH_3COOH in the scaffolds [30,33]. For the LDH nanoplates (Fig. 1c), the peak at 3506 cm^{-1} corresponded to the stretching vibration of –OH group and interlamellar water. The strong peak at 1380 cm^{-1} and weak peak at 661 cm^{-1} were ascribed to the intercalated NO_3^- ions and metal-oxygen vibrations in the LDHs, respectively [52]. The main characteristic peaks of both CS and LDH were detected in the FTIR spectrum of the $SrFe_{12}O_{19}$-LDH/CS scaffolds (Fig. 1d)..

The $SrFe_{12}O_{19}$-LDH/CS composite scaffolds were prepared from a mixed solution containing CS, LDH powder, and $SrFe_{12}O_{19}$ nanoparticles via freeze-drying (Fig. 2). The low-resolutional SEM images indicates that the LDH/CS and $SrFe_{12}O_{19}$-LDH/CS composite scaffolds possessed layered macropores with sizes of 50–100 μm (Fig. 2a and e). The layers in the $SrFe_{12}O_{19}$-LDH/CS scaffolds were 10.5 ± 0.8 per millimetre. It was found that the plate-like LDH nanoparticles had a thickness of approximately 30 nm, and the pieces were stacked to form flower clusters at a high resolution (Fig. 2b and f). The $SrFe_{12}O_{19}$ nanoparticles exhibited a flake-like structure with a thickness of approximately 40 nm and a width between 50 and 130 nm (Fig. 2c and d). The above data was confirmed through the Mg, Al, Sr, and Fe distribution images (Fig. 3a–d). The EDS patterns indicate that the $SrFe_{12}O_{19}$-LDH/CS scaffold was composed of C, O, Mg, Al, Sr, and Fe. The C element was mainly ascribed to CS, while the O element originated from LDH, CS, and $SrFe_{12}O_{19}$ (Fig. 3e and f).

3.2. Magnetic property, mechanical property and ion-release performance of $SrFe_{12}O_{19}$-LDH/CS scaffold

Magnetic fields play a key role in promoting cell proliferation and osteogenic differentiation [28,29]. In order to enhance the

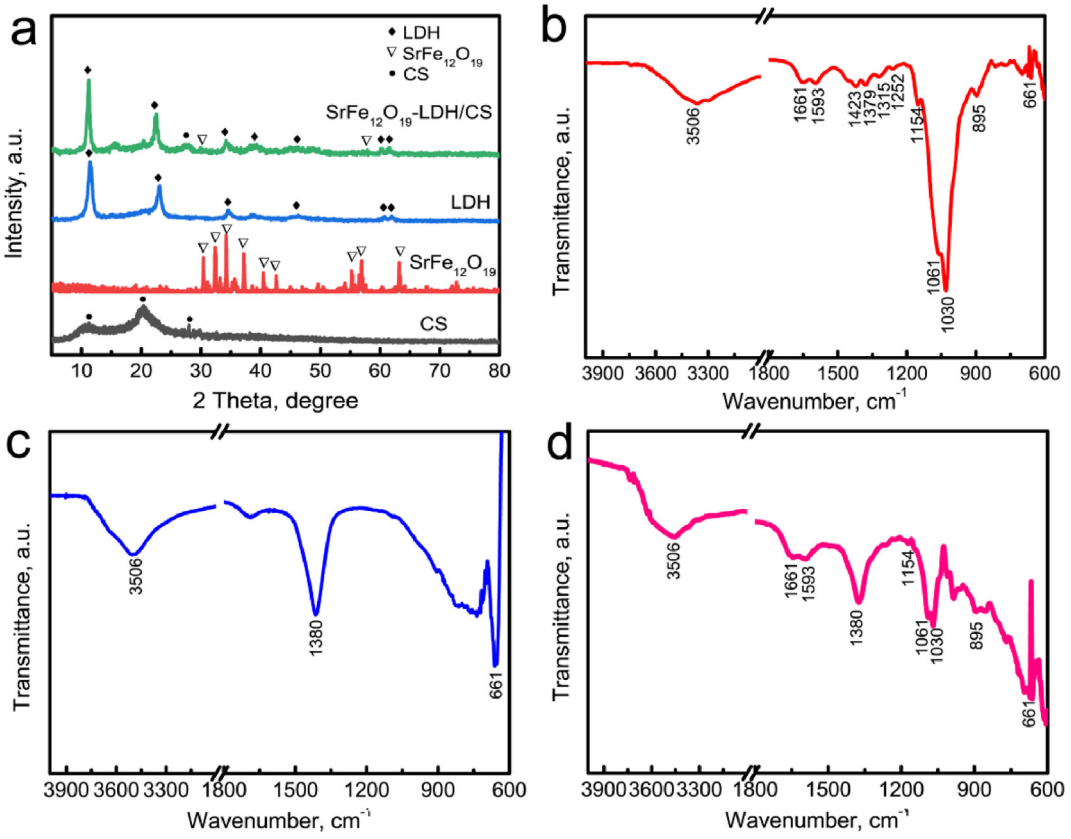

Fig. 1. (a) XRD pattern of CS powders, $SrFe_{12}O_{19}$ nanoparticles, LDH/CS scaffolds and $SrFe_{12}O_{19}$-LDH/CS scaffolds. FTIR spectra of different samples: (b) CS powders, (c) LDH nanoplates and (d) $SrFe_{12}O_{19}$-LDH/CS scaffolds.

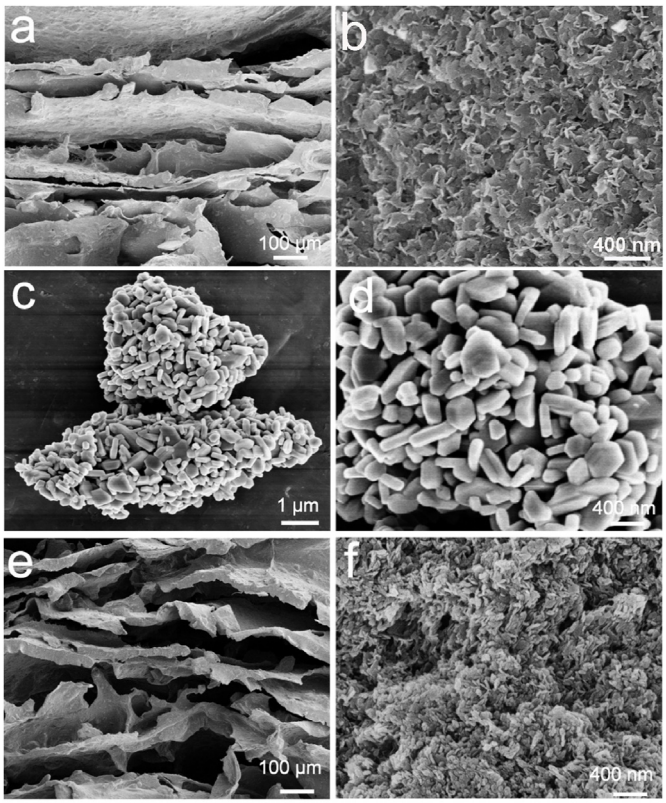

Fig. 2. (a, b) SEM images of the LDH/CS scaffold. (c, d) SEM images of $SrFe_{12}O_{19}$ nanoparticles. (e, f) SEM images of $SrFe_{12}O_{19}$-LDH/CS scaffolds.

pro-osteogenesis property, M-type $SrFe_{12}O_{19}$ hexagonal ferrites with high magnetocrystalline anisotropy were added in the bone scaffolds. The magnetic properties of $SrFe_{12}O_{19}$ nanoparticles and $SrFe_{12}O_{19}$-LDH/CS composite scaffolds were evaluated by a VSM (Fig. 4a and b). According to hysteresis loop, the coercivity values of $SrFe_{12}O_{19}$ nanoplates and $SrFe_{12}O_{19}$-LDH/CS scaffolds were 5756 Oe and 4800 Oe, respectively. The incorporation of $SrFe_{12}O_{19}$ nanoparticles endowed the $SrFe_{12}O_{19}$-LDH/CS scaffolds with the saturation magnetization of 3.82 emu/g (Fig. 4a).

The curves in Fig. 4d and e indicated the release characteristics of Mg^{2+} and Sr^{2+} ions from the $SrFe_{12}O_{19}$-LDH/CS composite scaffolds. The release rate of the two ions increased rapidly in the first 12 h, gradually decreased, then finally reached an equilibrium state. After soaking for 100 h, the concentration of the ions in the solution remained unchanged. The concentration of Mg^{2+} and Sr^{2+} ions after 120 h were determined to be 6.0 μM and 2.6 μM, respectively. Although the Mg^{2+}, Al^{3+}, Sr^{2+} and Fe^{3+} metal cations existed in the $SrFe_{12}O_{19}$-LDH/CS scaffolds, the concentrations of Al^{3+} and Fe^{3+} ions were lower than the detection limit of ICP. Under physiological conditions with pH = 7.4, the excess Al^{3+} and Fe^{3+} ions may react with OH^- ions to form $Al(OH)_3$ and $Fe(OH)_3$. The solubility product constants (K_{sp}) of $Al(OH)_3$ and $Fe(OH)_3$ are 1.3×10^{-33} and 4.0×10^{-38} at a room temperature, respectively. The saturated concentrations of Al^{3+} and Fe^{3+} ions were calculated as 8.20×10^{-15} M and 2.52×10^{-18} M, respectively. Such the low Al^{3+} and Fe^{3+} concentrations did not cause any toxicity to human cells and organs [53, 54].

The macropores in bone scaffolds played an important role in osteogenesis, osteoconductive and osteoinductive [30]. In order to avoid destroying the layered macropores, the nacre-mimetic porous scaffolds should have appropriate mechanical strengths. The compressive strengths of the LDH/CS and $SrFe_{12}O_{19}$-LDH/CS scaffolds were tested under the same conditions (Fig. 4c). As the compression displacement increased, the compression stress of the LDH/CS and $SrFe_{12}O_{19}$-LDH/CS scaffolds gradually increased. The ordered layer structure could be damaged at the first stage with the increase of the compression stress. Fig. 4c indicated that the compressive strengths to destroy the layered macropores were approximately 0.16–0.18 MPa. Because both the LDH/CS and $SrFe_{12}O_{19}$-LDH/CS scaffolds were organic-inorganic nanohybrid materials, their failure points were not reached even under much high compression stress.

3.3. Cytotoxicity and osteoinductivity of the $SrFe_{12}O_{19}$-LDH/CS scaffold in vitro

The above-mentioned extraction of scaffold (100μl/well) was cultured in MC-3T3-E1 cells (10^4 in 96-well) for 1, 2, 3 and 4 days, and the cytotoxicity and proliferation were detected after using CCK-8. CCK-8 experiment showed that the $SrFe_{12}O_{19}$-LDH/CS scaffold was not toxic to cells as cell proliferation was unaffected (Fig. 5a). In vitro, in order to

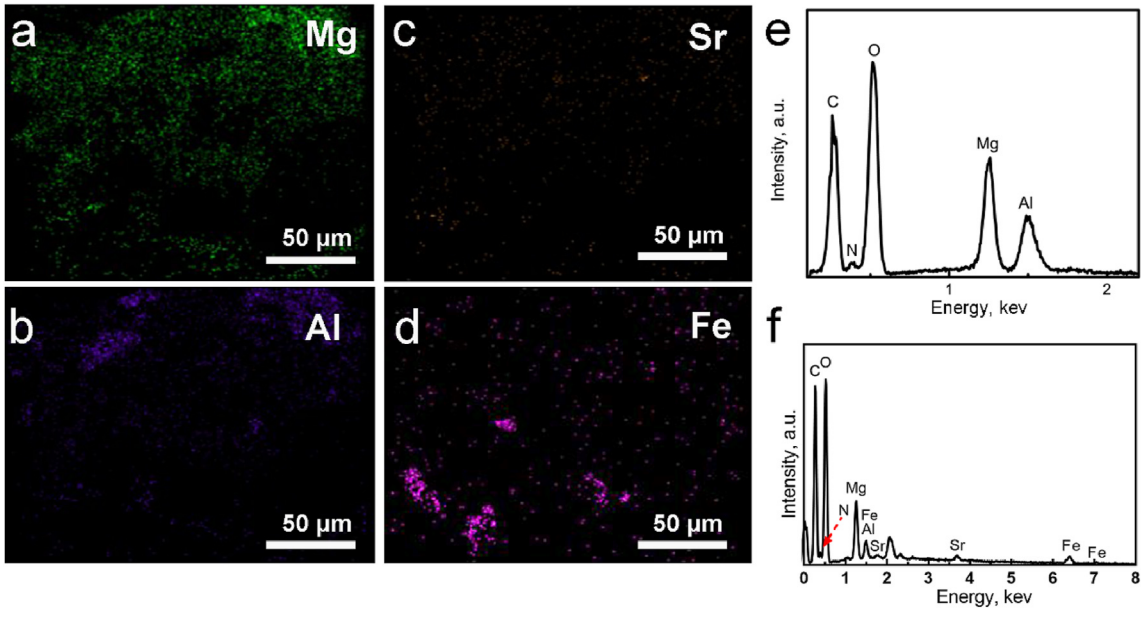

Fig. 3. (a–d) Element distribution images of Mg, Al, Sr, and Fe. (e–f) EDS spectra of (e) LDH/CS scaffolds. (f) $SrFe_{12}O_{19}$-LDH/CS scaffolds.

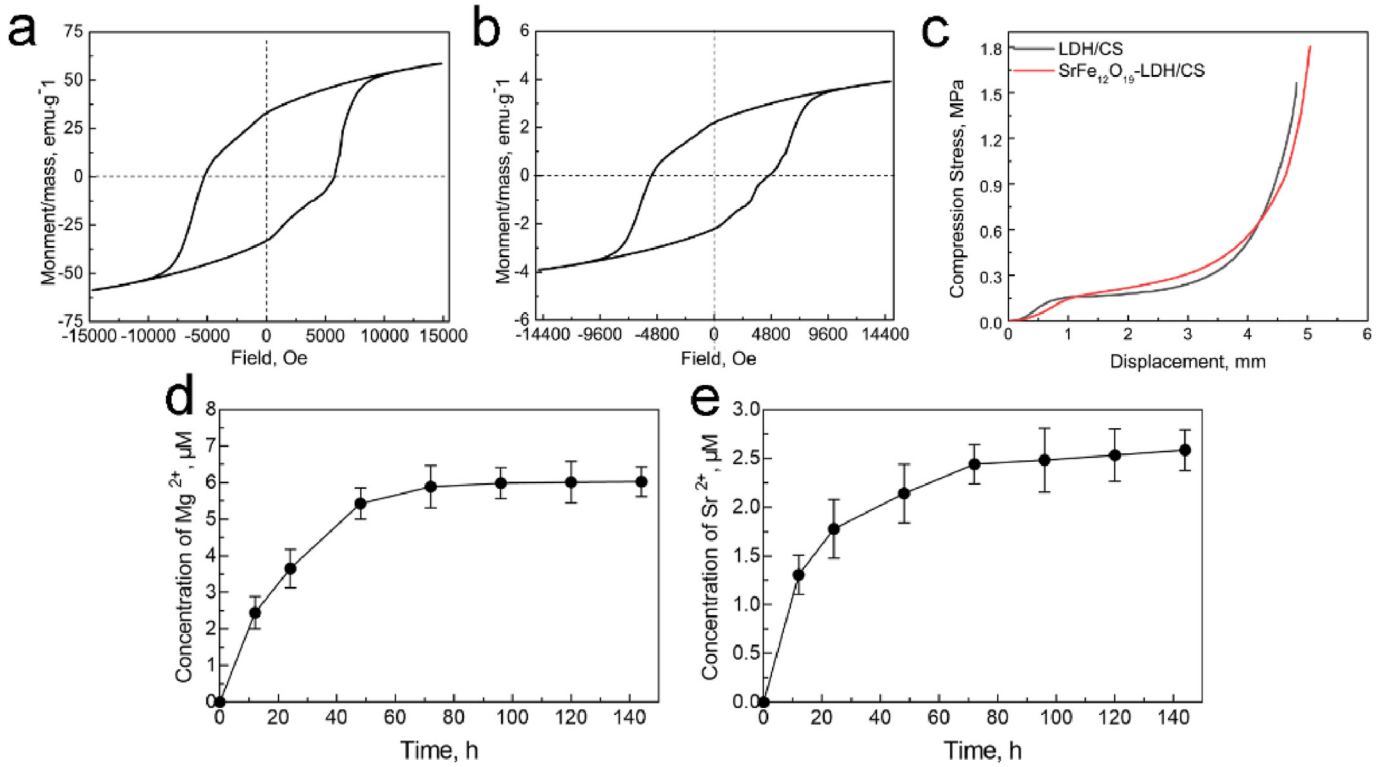

Fig. 4. (a) Magnetic hysteresis loops of $SrFe_{12}O_{19}$; (b) Magnetic hysteresis loops of $SrFe_{12}O_{19}$-LDH/CS composite scaffolds; (c) Compression properties of LDH/CS and $SrFe_{12}O_{19}$-LDH/CS scaffolds; (d, e) Mg^{2+} and Sr^{2+} release curve of $SrFe_{12}O_{19}$-LDH/CS composite scaffolds.

further verify the bone-inducing and mineralizing abilities of each group of scaffolds, ALP and ARs staining were performed. Fig. 5b shows the ALP staining of the control, the LDH/CS and the $SrFe_{12}O_{19}$-LDH/CS for 7 d. Compared to the other groups, the cells in the $SrFe_{12}O_{19}$-LDH/CS scaffolds showed the highest activity (Fig. 5d). The LDH/CS scaffold group had higher activity than the control group but was less than that of the $SrFe_{12}O_{19}$-LDH/CS scaffold group. Similar results were observed with Alizarin red staining for 21 d (Fig. 5c). It indicates the late mineralization of osteoblasts. The LDH/CS and $SrFe_{12}O_{19}$-LDH/CS scaffolds showed higher Alizarin activity than the control, with the $SrFe_{12}O_{19}$-LDH/CS scaffolds showing the highest activity (Fig. 5e). Scanning electron microscope observation of hBMSCs morphology on the LDH/CS and S $SrFe_{12}O_{19}$-LDH/CS scaffolds (Fig. 5f). The hBMSCs on the LDH/CS scaffold had protruded filamentous pseudopodia and are closely bound to the surface of the scaffold. The morphology of the hBMSCs on the scaffold was well-distributed, similar to that on the LDH/CS scaffold. These results showed that $SrFe_{12}O_{19}$-LDH/CS scaffolds had no significant effect on cell adhesion.

The above phenomenon observed that $SrFe_{12}O_{19}$-LDH/CS scaffolds can promote osteoblast differentiation. To this end, we further explore the molecular mechanism of the above phenomenon. By RT-PCR and WB, the osteoblast-specific genes (Fig. 5g–i) and proteins (Fig. 5j-n) were detected, respectively. Compared to the control, the genes expression (*Col1*, *Bmp-2*, and *Runx2*) in the LDH/CS and $SrFe_{12}O_{19}$-LDH/CS were higher. Similarly, the osteoblast-related proteins (Bmp-2, Runx2, Col-1, and P-Smad1/5) were higher in the LDH/CS and $SrFe_{12}O_{19}$-LDH/CS. *Col1* is an important part of bone tissue formation, which promotes calcium and phosphorus deposition and accelerates the calcification of new bone tissue. *Runt-related transcription factor 2 (Runx2)* is a specific transcription factor that regulates the differentiation of mesenchymal stem cells into osteoblasts. *Bmp-2 and P-Smad1/5* are target proteins in the classical pathway of osteoblast differentiation. We speculated that it was possible that the Mg^{2+} and Sr^{2+} ions from the $SrFe_{12}O_{19}$-LDH/CS scaffolds promoted osteoblast differentiation by activating the P-Smad signaling pathway [55–58]. In terms of osteoinductive-related genes and proteins, the osteoinductive ability presents: the control group < the LDH/CS group < the $SrFe_{12}O_{19}$-LDH/CS group. At the same time, the $SrFe_{12}O_{19}$-LDH/CS scaffold had a more obvious effect on promoting osteoblast differentiation, which may be due to the synergistic effect of Mg^{2+} and Sr^{2+}.

3.4. The effect of $SrFe_{12}O_{19}$-LDH/CS scaffolds on osteoclast differentiation in vitro

Considering the host as a whole organism, the implantation of bioscaffolds may disrupt bone homeostasis. The maintenance of bone homeostasis requires both the mineralization of osteoblasts and bone resorption of osteoclasts. Therefore, our group further investigated the effect of the LDH/CS and $SrFe_{12}O_{19}$-LDH/CS scaffolds on osteoclast differentiation. Tartrate-resistant acid phosphatase (TRAP) is a marker protease during osteoclast differentiation and is evenly distributed in osteoclasts. We cultured BMMs (96-well, 10^4/per) for 7 d using the above-mentioned extract. Then use the TRAP kit to detect. TRAP-positive cells are marked by three fused nuclei. TRAP staining (Fig. 6a–c) revealed that the TRAP-positive and the area in the LDH/CS and $SrFe_{12}O_{19}$-LDH/CS groups were notably reduced. At the same time, the osteoclast cytoskeleton F-actin has also been verified, which is an important marker of osteoclast fusion. Similar results were observed for F-actin staining (Fig. 6d and e). The inhibitory effect of $SrFe_{12}O_{19}$-LDH/CS on osteoclasts was significantly stronger than that of LDH/CS. This indicated that the Sr^{2+} released from the $SrFe_{12}O_{19}$-LDH/CS scaffolds would further inhibit the formation of osteoclasts. Therefore, our group further detected the expression of osteoclast-specific proteins (C-FOS, NFATc1, Cath-K, p–NF–κB and *p*-iKBα) via western blotting (Fig. 6f–k). C-FOS protein, NFATc1 protein and NF-κB protein jointly participate in the classical pathway regulating osteoclast differentiation. Cathepsin K (Cath-K) is a specific protein in osteoclast differentiation. Fig. 6f shows that C-FOS, NFATc1 and Cath-K protein expression was suppressed in the LDH/CS

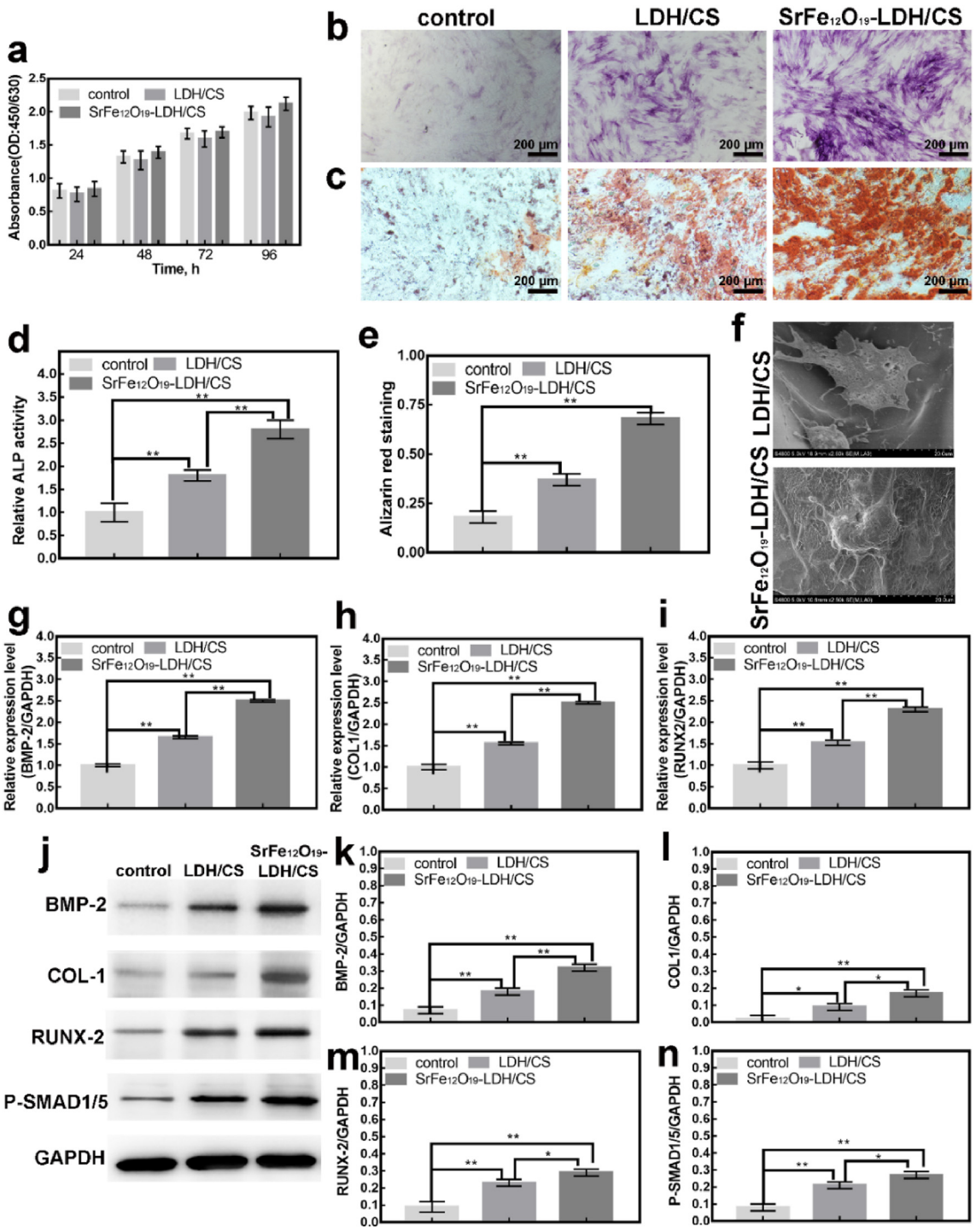

Fig. 5. (a) CCK8 experiments of the control, the LDH/CS scaffold and the $SrFe_{12}O_{19}$-LDH/CS scaffold at different time points; (b, c) ALP for 7 d and ARS for 21 d; (d, e) Statistical Analysis of b, c; (f) SEM for 24 h; (g, h, i) RT-PCR: expression of osteoblast genes for 7 d; (j) WB: Bmp-2, Col-1, Runx-2 and P-Smad1/5 proteins for 7 d; (k, l, m, n) Statistical Analysis. *P < 0.05, **P < 0.01.

and $SrFe_{12}O_{19}$-LDH/CS groups. C-FOS and NFATc1 are critical factors in the early differentiation of osteoclasts. The study found that the *p*-IKBα protein and the *p*-NFκB protein were significantly inhibited in the LDH/CS and $SrFe_{12}O_{19}$-LDH/CS groups (Fig. 6f). *p*-IKBα is a key protein in the NF-κB signaling pathway. The above results suggest that Mg^{2+} and Sr^{2+} released in the LDH/CS and $SrFe_{12}O_{19}$-LDH/CS groups inhibited osteoclast differentiation by inhibiting the phosphorylation of the IKBα protein. Experiments also showed that the inhibitory effect of $SrFe_{12}O_{19}$-LDH/CS was significantly stronger than that of LDH/CS (Fig. 6g–k). In the experiment of inhibiting osteoclast differentiation, it was found that its effect was presented: control group < LDH/CS group < $SrFe_{12}O_{19}$-LDH/CS group. Therefore, Mg^{2+} and Sr^{2+} may have a synergistic effect.

3.5. Osteogenic activities of the $SrFe_{12}O_{19}$-LDH/CS scaffolds in vivo

Bilateral critical-size calvarial defect models were used to evaluate the osteogenic activity of the control, LDH/CS, and $SrFe_{12}O_{19}$-LDH/CS *in vivo* (Fig. 7). The diameter of the skull transfora is 5 mm and the thickness

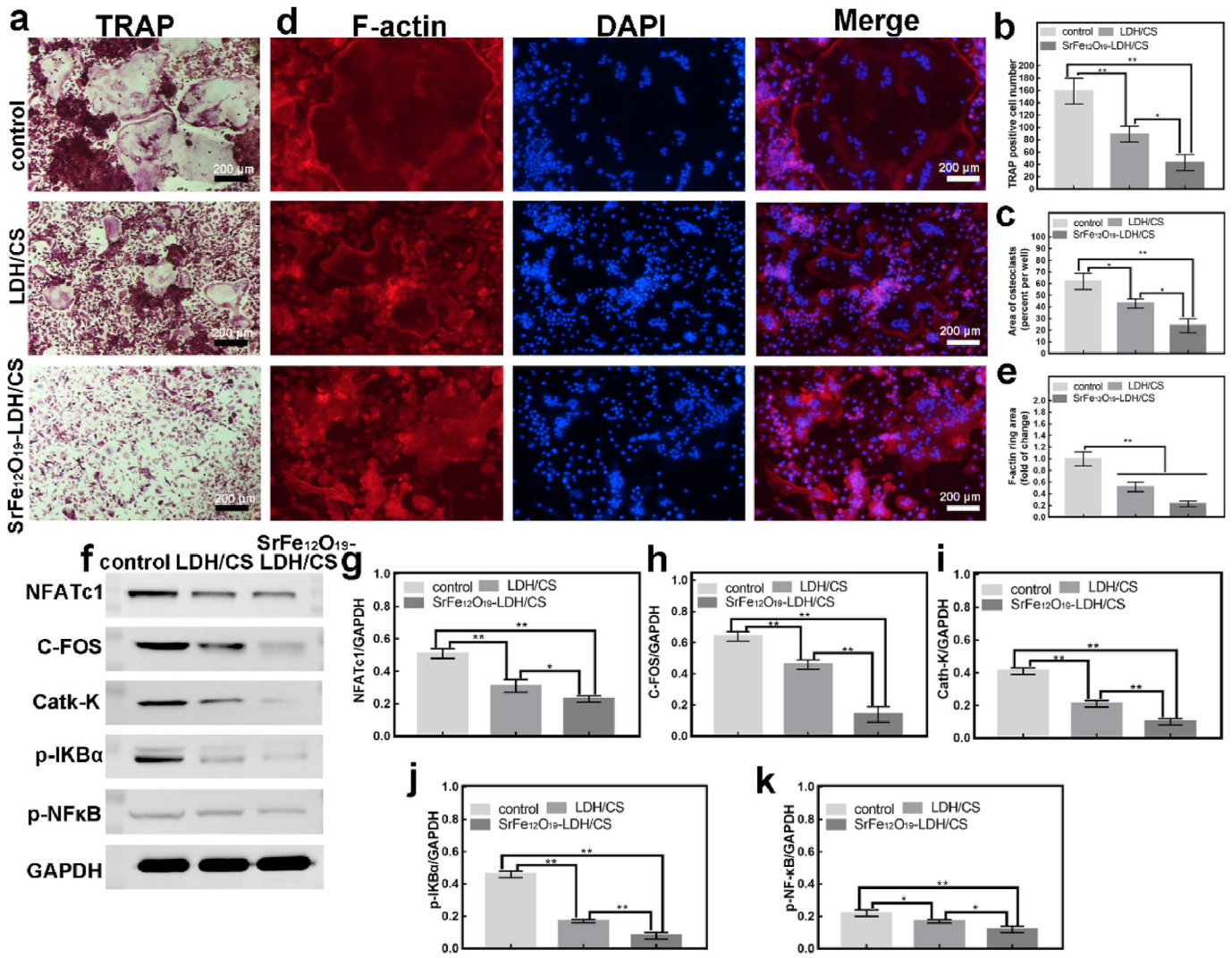

Fig. 6. (a, b, c) TRAP staining for 7 d, the number and the area of TRAP-positive cells; (d, e) F-actin for 7 d, DAPI and Merge, statistical analysis; (f) WB: NFATc1, C-FOS, Cath-K, *p*-IKBα and *p*-NFκB proteins for 7 d; (g, h, i, j, k) Statistical Analysis. *P < 0.05, **P < 0.01.

is 2 mm. The red dotted circle indicates the size of the *trans*-hole, which matches the scaffold material. All rats were housed in a uniform environment setting: temperature: 20–26 °C, relative humidity: 70%, light intensity ≥200 lux, and free access to water and food. All rats were kept in this environment for 3 months. After three months, they were euthanized. After that, the part of the skull of interest at the top of the soft tissue separation was removed and placed in 4% paraformaldehyde, waiting for subsequent experiments. Fig. 7a shows a μCT image. New bone tissue formed in all three groups. The amount of new bone in the LDH/CS and $SrFe_{12}O_{19}$-LDH/CS groups was higher than that in the control. Moreover, the amount of new bone tissue in the $SrFe_{12}O_{19}$-LDH/CS group was higher than that in the LDH/CS group. Once again, it was demonstrated that Mg^{2+} and Sr^{2+} could accelerate bone formation *in vivo* and that they may have synergistic effects. Compared to the control (9.21 ± 5.23%), the BV/TV values in the LDH/CS (35.31 ± 3.15%) and $SrFe_{12}O_{19}$-LDH/CS (59.21 ± 4.01%) groups were significantly greater (Fig. 7b). Additionally, the LDH/CS (0.35 ± 0.09 g/cm^3) and $SrFe_{12}O_{19}$-LDH/CS (0.54 ± 0.06 g/cm^3) groups had higher BMD values than the control (0.16 ± 0.06 g/cm^3) group (Fig. 7c). The growth rates of the new bones were also analyzed using sequence fluorescence Analysis (Fig. 7d). The distance between these two fluorescent lines represents the new bone tissue that formed during this time. After data analysis (Fig. 7e), the new bone growth rate in the LDH/CS and $SrFe_{12}O_{19}$-LDH/CS groups reached 0.36 ± 0.07 μm/d and 0.58 ± 0.12 μm/d, respectively, which were higher than that of the control group (0.14 ± 0.06 μm/d). HE staining (Fig. 7f) showed results similar to those of the μCT experiment. In HE staining, a large number of collagen fibers can be found aggregated between the lamellar scaffolds.

The above demonstrated that the $SrFe_{12}O_{19}$-LDH/CS scaffolds could promote bone mineralization. However, the bone homeostasis depends on the OPG/RANKL ratio. Thus, we investigated whether $SrFe_{12}O_{19}$-LDH/CS scaffolds affected the expression of OPG/RANKL by immunofluorescence. Fig. 8a and b shows that the fluorescence of OPG protein and RANKL protein. The green picture represents the OPG protein content: $SrFe_{12}O_{19}$-LDH/CS group > LDH/CS group > CS group; while the red picture represents the RANKL protein content: $SrFe_{12}O_{19}$-LDH/CS group < LDH/CS group < CS group. The trend is just opposite to the OPG protein expression. Therefore, we speculate that the trend of OPG/RANKL will be $SrFe_{12}O_{19}$-LDH/CS group > LDH/CS group > CS group, similar to the trend in the expression of neovascularization indicators (Fig. 8c). Finally, the samples for the expression of osteoblast differentiation-related proteins (Runx-2 and COL-1) and inflammatory factors (IL-1β and TNF-α) (Fig. 8d–g) were tested. It showed that the protein expression of RUNX-2 and COL-1 (Fig. 8d and e) in the LDH/CS and $SrFe_{12}O_{19}$-LDH/CS groups increased while the expression of inflammation-related proteins IL-1β and TNF-α (Fig. 8f and g) decreased.

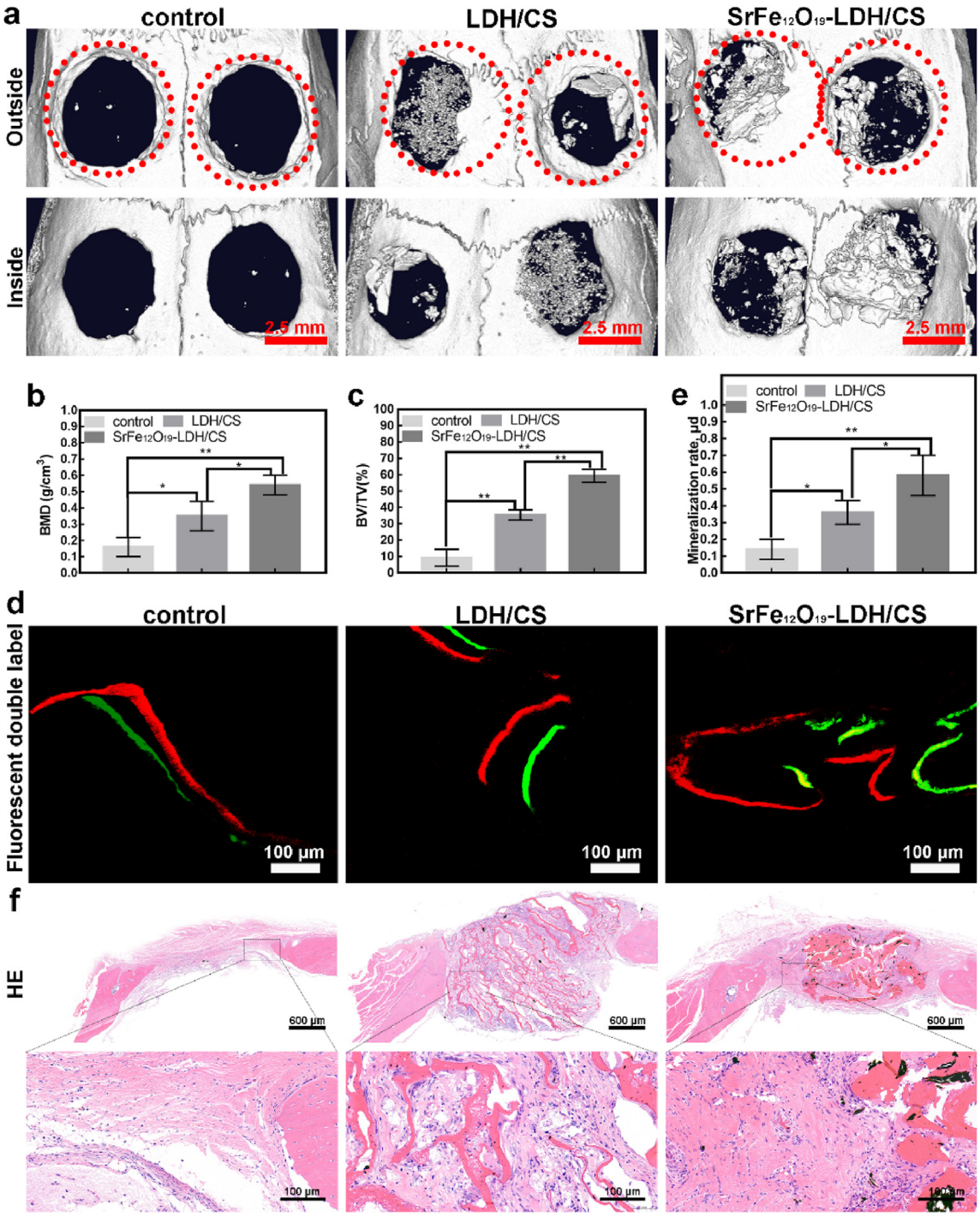

Fig. 7. (a) Micro-CT; (b, c) BMD and BV/TV; (d, e) Red represents alizarin red and green represents calcein, and the distance between them is new bone tissue; mineralization rate; (f) H&E; *p < 0.05; **p < 0.01. (For interpretation of the references to colour in this figure legend, the reader is referred to the Web version of this article.)

4. Discussion

The repair of different bone defects has always been an important yet difficult problem in orthopedics, especially in patients with bone homeostasis imbalance [7]. A preferred criteria for clinical treatment of bone defects caused by the above factors is autologous bone transplantation, but it is difficult to meet these needs owing to limited bone sources for transplantation [3,8]. However, allogeneic bone transplantation has shortcomings, such as slow healing, immune rejection, susceptibility to infection, and an increased risk of spreading diseases. In recent years, the addition of different metal elements into biomaterials and the formation of scaffolds into morphological structures conducive to cell growth have been rapidly developed [16]. However, further improvement of the osteogenic ability of biomaterials, the expression of effective biomolecules, and the clinical safety of these materials is a problem to be solved.

Inspired by the layered features of nacre, several fabrication approaches such as shear-flow-induced alignment [59], fluidics-enabled assembling [60] and freeze-casting [61] have been developed to construct layered nanohybrid materials. In this work, nacre-mimetic

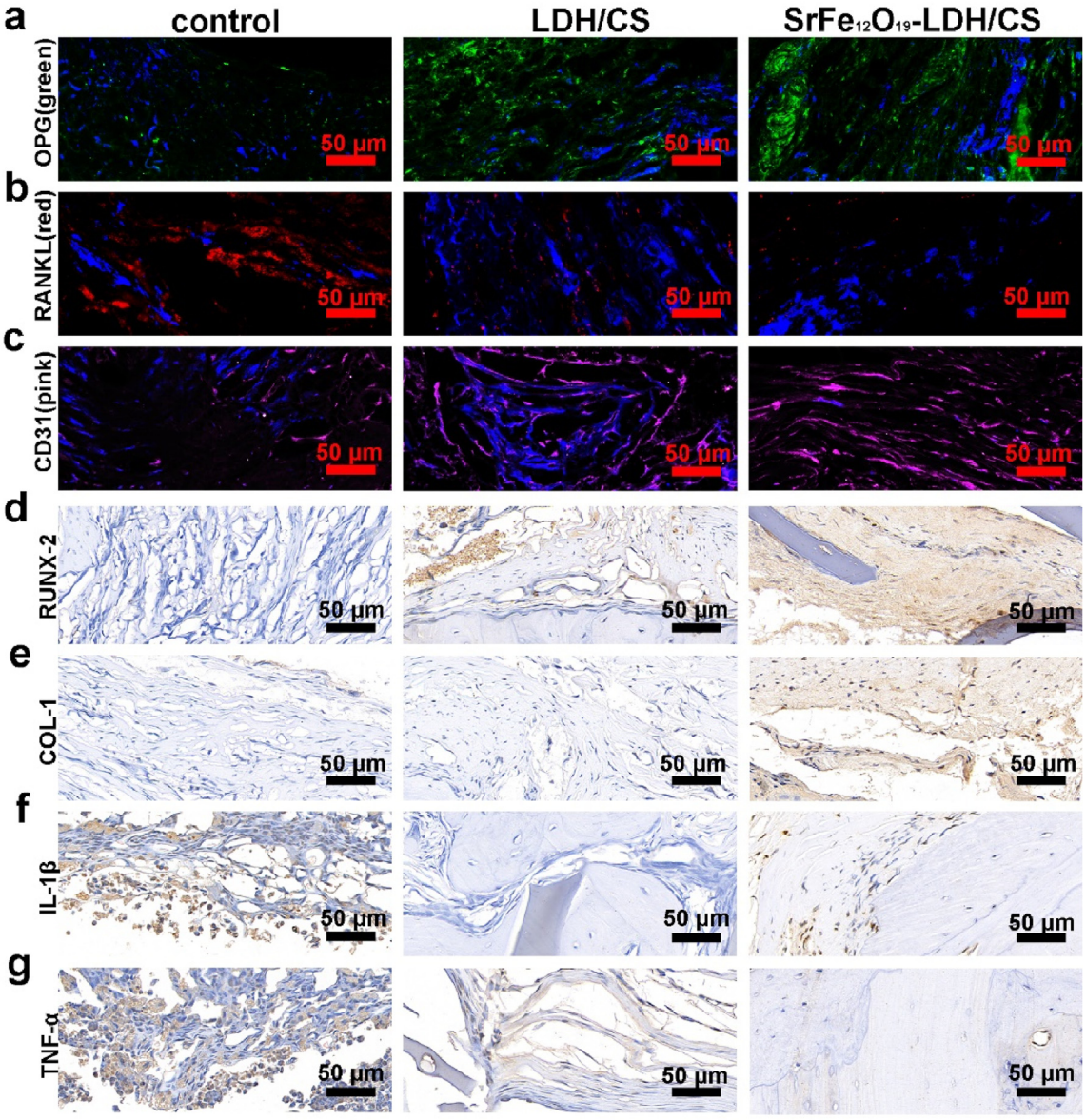

Fig. 8. (a, b) DAPI is shown in blue; OPG is shown in green; RANKL is shown in red; (c) CD31 is shown in pink and represents new blood vessels. (d, e) Osteogenesis-related proteins (RUNX-2 and COL1) immunohistochemistry; (f, g) IL-1β and TNF-α immunohistochemistry

$SrFe_{12}O_{19}$-LDH/CS layered scaffolds were fabricated according to the following steps: (i) the preparation of the composite slurry by the addition of $SrFe_{12}O_{19}$ nanoplates and LDH nanoplates in a CS solution, and (ii) the formation of nacre-mimetic $SrFe_{12}O_{19}$-LDH/CS layered scaffolds via the freeze-drying treatment of the composite slurry. During the freezing procedure, the as-formed ice crystals expelled the $SrFe_{12}O_{19}$ and LDH nanoparticles, and thus produced lamellar structure parallel to the movement of freezing front [61]. The freeze-drying treatment caused the sublimation of the layered ice crystals, leading to the formation of layered macropores (Fig. 2e). Because the hydroxyl groups and crystal water in LDHs could be combined with CS via hydrogen bonding (Fig. 2b), the LDH nanoplates were embed in the CS matrix through a self-assembly process. The LDH/CS and $SrFe_{12}O_{19}$-LDH/CS scaffolds were arranged in a layered structure (Fig. 2), indicating that the $SrFe_{12}O_{19}$ did not affect the layered structure. The pure CS porous scaffolds showed the ductile characteristic, so their compressive strength was not great enough to meet the clinical demand [30]. Interestingly, the $SrFe_{12}O_{19}$-LDH/CS layered scaffolds displayed a "brick and mortar" structure with the $SrFe_{12}O_{19}$ nanoparticles and LDH nanosheets as inorganic fillers and CS as organic matrices. The organic-inorganic nanohybid architecture endowed the nacre-mimetic scaffolds with appropriate mechanical property. The compressive strengths to destroy the layered macropores of the LDH/CS and $SrFe_{12}O_{19}$-LDH/CS layered scaffolds arrived at 0.16–0.18 MPa. Our previous work indicated that the La-doped LDH/CS porous scaffolds had the similar compressive strength of approximately 0.21 MPa [20]. Fortunately, the layered macropores of the LDH/CS and $SrFe_{12}O_{19}$-LDH/CS layered scaffolds provided enough mechanical strength for the invasion and migration of macrophages and osteoblasts. Even after 12 weeks of post-operation, the undegraded scaffolds still possessed a layered structure (Fig. 7f).

In this article, scholars also mention that biomaterials entering the body need to recruit a large number of macrophages, centrocyte, and lymphocytes to aggregate, which will trigger a local immune response and inhibit the differentiation and mineralization of osteoblasts [62,63]. One of the goals of our group was to develop layered $SrFe_{12}O_{19}$-LDH/CS nanohybrid scaffolds to prevent the aggregation of macrophages and avoid triggering local immune response through the release of inflammatory factors. Inflammatory factors promote the differentiation of

macrophages into osteoclasts [23]. Fig. 6 illustrates that the layered $SrFe_{12}O_{19}$-LDH/CS nanohybrid scaffolds can inhibit the osteoclasts differentiation. A research group found that layered $SrFe_{12}O_{19}$-LDH/CS nanohybrid scaffolds inhibited the osteoclasts differentiation by the NF-κB signaling pathway. Osteoclast differentiation further releases pro-inflammatory factors. Zhai et al. reported that Mg^{2+} and Sr^{2+} ions could inhibit RANKL-mediated osteoclast differentiation. By examining the ion release profile of the $SrFe_{12}O_{19}$-LDH/CS nanohybrid scaffolds, The results showed that the Sr^{2+} ion concentration reached approximately 2.6 μM and the Mg^{2+} ion concentration reached 5.8 μM after 120 h (Fig. 4d and e). The study found that Mg^{2+} and Sr^{2+} can synergistically inhibit osteoclast differentiation. Animal experiments showed that the OPG/RANKL ratio (Fig. 8a and b) could also be regulated by the $SrFe_{12}O_{19}$-LDH/CS nanohybrid scaffolds. The local OPG/RANKL protein ratio is a crucial factor in regulating osteoclast differentiation. Immunohistochemical evaluation of the bone tissue also showed the inhibition of inflammatory factors (Fig. 8f and g).

Another goal of our group in developing layered $SrFe_{12}O_{19}$-LDH/CS nanohybrid scaffolds was to accelerate osteoblast differentiation and mineralization to induce endochondral osteogenesis. As mentioned in our background section, static magnetic field (SMF) was shown to be a new physical stimulation strategy to induce cell proliferation and osteogenic differentiation. Hiroko Kotani et al. demonstrated intragranular and ectopic bone formation upon SMF stimulation. Interestingly, the direction in which the bone is formed is parallel to the magnetic field [28]. In addition, the breakthrough point of our research group is the osteoinductive effect of Sr ions on osteoblasts. Osteogenesis is divided into main processes: endochondral osteogenesis and intraperitoneal osteogenesis. Collagen fibers were pale pink in tissue sections, and elastic fibers were bright pink (Fig. 7f). These results show the formation of the extracellular matrix in the layered $SrFe_{12}O_{19}$-LDH/CS nanohybrid scaffolds. Collagen fibers are an important component of the extracellular matrix, while the cartilage is composed of many collagen fibers. HE staining revealed that the collagen in the scaffold material might be an important extracellular matrix component in later endochondral osteogenesis. Therefore, the designed layered space structure in the $SrFe_{12}O_{19}$-LDH/CS nanohybrid scaffold (Fig. 2a, e) was conducive to the growth of collagen fibers and provided a more suitable growth environment for bone. In addition, the layered $SrFe_{12}O_{19}$-LDH/CS nanohybrid scaffold contained LDH and Sr^{2+} ions. Zhai and Wu et al. reported that Mg^{2+} and Sr^{2+} ions in LDH could regulate osteoblast differentiation. Fig. 5 illustrates that the layered $SrFe_{12}O_{19}$-LDH/CS nanohybrid scaffold can increase alkaline phosphatase activity and accelerate bone mineralization through the P-Smad signaling pathway. Histomorphological analysis showed that Sr^{2+} ions could promote mineralization of the extracellular matrix in the layered scaffolds, which was in line with the original intention of the material design. Next, the immunohistochemical analysis of bone tissue sections for Runx-2 and COL1 expression were performed. Immunohistochemistry revealed that Runx-2 protein was increased in the layered structures (Fig. 8d). Runx-2 is a key transcription factor for the osteoblasts differentiation, to promote the maturation of chondrocytes. Therefore, the presence of Sr^{2+} ions also verified the mineralization of the extracellular matrix in the layered scaffolds. In addition, COL1 is a key protein in osteogenic differentiation. It showed that COL1 protein expression was increased in the layered $SrFe_{12}O_{19}$-LDH/CS nanohybrid scaffold. This phenomenon also proves that the presence of Sr in the layered $SrFe_{12}O_{19}$-LDH/CS nanohybrid scaffold can accelerate osteoblast mineralization and endochondral osteogenesis. In conclusion, the layered $SrFe_{12}O_{19}$-LDH/CS nanohybrid scaffold can be used as a bioscaffold to regulate local bone homeostasis and accelerate bone regeneration.

Interestingly, in the local magnified picture of HE, a large number of collagen fibers packed between the lamellar scaffolds could be found. And it was also confirmed in the follow-up histochemistry that the collagen fibers inside the lamellar structure contain a large amount of type 1 collagen. Type 1 collagen is an important component of the extracellular matrix of bone tissue. In addition, HE showed that a large number of macrophages gathered around the $SrFe_{12}O_{19}$-LDH/CS scaffold. Macrophage nuclei appear larger and dark blue in HE staining. After the scaffold is implanted, on the one hand, the internal buffer environment of the body will accelerate its degradation, and on the other hand, macrophages can also mediate the degradation. The scaffold material will release Sr ions and Mg ions in the huge buffer environment inside the body [64]. When the scaffold releases ions, the scaffold will also accelerate the degradation simultaneously. In addition, macrophages possess powerful phagocytosis [65,66]. It can be seen from HE that there are a large number of macrophages around, and macrophages will also adhere to the surface of the scaffold and slowly phagocytose the scaffold.

5. Conclusion

To effectively solve the problem of bone homeostasis caused by implantation *in vivo*, we successfully fabricated a layered nano-$SrFe_{12}O_{19}$-LDH/CS nanohybrid scaffold containing nano-Sr-LDH nanoplates ordered on a CS matrix and a CS matrix with a layered structure. The layered structure of the scaffold was conducive to the adhesion and pseudopodia migration of macrophages and bone marrow mesenchymal stem cells, promoted the formation of the extracellular matrix (collagen fibers), and accelerated the mineralization of new bone tissue. LDH and Sr^{2+} ions were added to the layered structure. We found that Mg^{2+} and Sr^{2+} released from the scaffold could regulate the release of local inflammatory factors and inhibit the osteoclasts differentiation. Hence, this scaffold plays an early protective role in fibrous tissue encapsulation caused by the immune response. In addition, we found that the release of Mg^{2+} and Sr^{2+} ions from the scaffold can regulate the expression of the transcription factor Runx-2, which could promote the formation of collagen fibers and accelerate the mineralization of bone marrow mesenchymal stem cells. The release of Mg^{2+} and Sr^{2+} from the scaffold regulates the local OPG/RANKL ratio, maintaining the local bone homeostasis between osteoblasts and osteoclasts. In our future research, we will focus on the following: solving the problem of matching the degradation of scaffold materials with the mineralization of new bone tissue, determining whether Sr^{2+} ions could promote the formation of Haval tubules, and elucidating the mechanism of angiogenesis in new bone tissue.

Data availability

These data are available from the corresponding authors upon reasonable request.

Credit author statement

CQZ and YPG provided guidance for this study and designed the specific procedures of the trial. QFK and WTJ wrote the manuscript. YWG and ZHF completed the specific process of the experiment.

Declaration of competing interest

The authors declare that they have no known competing financial interests or personal relationships that could have appeared to influence the work reported in this paper.

Acknowledgments

This research was supported by The National Key Research and Development Program of China (No. 2018YFC1106300), National Natural Science Foundation of China (No. 82002270).

References

[1] W. Zou, X. Li, N. Li, T. Guo, Y. Cai, X. Yang, J. Liang, Y. Sun, Y. Fan, A comparative study of autogenous, allograft and artificial bone substitutes on bone regeneration and immunotoxicity in rat femur defect model, Regen Biomater 8 (1) (2021), rbaa040.

[2] A. Patel, S.H. Zaky, K. Schoedel, H. Li, V. Sant, E. Beniash, C. Sfeir, D.B. Stolz, S. Sant, Design and evaluation of collagen-inspired mineral-hydrogel nanocomposites for bone regeneration, Acta Biomater. 112 (2020) 262–273.

[3] E. Garcia-Gareta, M.J. Coathup, G.W. Blunn, Osteoinductive of bone grafting materials for bone repair and regeneration, Bone 81 (2015) 112–121.

[4] T. Lin, J. Pajarinen, A. Nabeshima, L. Lu, K. Nathan, E. Jamsen, Z. Yao, S.B. Goodman, Preconditioning of murine mesenchymal stem cells synergistically enhanced immunomodulation and osteogenesis, Stem Cell Res. Ther. 8 (1) (2017) 277.

[5] Y. Etani, K. Ebina, M. Hirao, K. Kitaguchi, M. Kashii, T. Ishimoto, T. Nakano, G. Okamura, A. Miyama, K. Takami, A. Goshima, T. Kanamoto, K. Nakata, H. Yoshikawa, Combined effect of teriparatide and an anti-RANKL monoclonal antibody on bone defect regeneration in mice with glucocorticoid-induced osteoporosis, Bone 139 (2020), 115525.

[6] W. Shen, B. Sun, C. Zhou, W. Ming, S. Zhang, X. Wu, CircFOXP1/FOXP1 promotes osteogenic differentiation in adipose-derived mesenchymal stem cells and bone regeneration in osteoporosis via miR-33a-5p, J. Cell Mol. Med. 24 (21) (2020) 12513–12524.

[7] B. Gao, R. Deng, Y. Chai, H. Chen, B. Hu, X. Wang, S. Zhu, Y. Cao, S. Ni, M. Wan, L. Yang, Z. Luo, X. Cao, Macrophage-lineage TRAP+ cells recruit periosteum-derived cells for periosteal osteogenesis and regeneration, J. Clin. Invest. 129 (6) (2019) 2578–2594.

[8] R. Dimitriou, E. Jones, D. McGonagle, P.V. Giannoudis, Bone regeneration: current concepts and future directions, BMC Med. 9 (2011) 66.

[9] D.P. Vasconcelos, A.P. Aguas, M.A. Barbosa, P. Pelegrin, J.N. Barbosa, The inflammasome in host response to biomaterials: bridging inflammation and tissue regeneration, Acta Biomater. 83 (2019) 1–12.

[10] A. Vishwakarma, N.S. Bhise, M.B. Evangelista, J. Rouwkema, M.R. Dokmeci, A.M. Ghaemmaghami, N.E. Vrana, A. Khademhosseini, Engineering immunomodulatory biomaterials to tune the inflammatory response, Trends Biotechnol. 34 (6) (2016) 470–482.

[11] L. Batoon, S.M. Millard, M.E. Wullschleger, C. Preda, A.C. Wu, S. Kaur, H.W. Tseng, D.A. Hume, J.P. Levesque, L.J. Raggatt, A.R. Pettit, CD169(+) macrophages are critical for osteoblast maintenance and promote intramembranous and endochondral ossification during bone repair, Biomaterials 196 (2019) 51–66.

[12] O.R. Mahon, D.C. Browe, T. Gonzalez-Fernandez, P. Pitacco, I.T. Whelan, S. Von Euw, C. Hobbs, V. Nicolosi, K.T. Cunningham, K.H.G. Mills, D.J. Kelly, A. Dunne, Nano-particle mediated M2 macrophage polarization enhances bone formation and MSC osteogenesis in an IL-10 dependent manner, Biomaterials 239 (2020), 119833.

[13] X. Xu, L. Xiao, Y. Xu, J. Zhuo, X. Yang, L. Li, N. Xiao, J. Tao, Q. Zhong, Y. Li, Y. Chen, Z. Du, K. Luo, Vascularized bone regeneration accelerated by 3D-printed nanosilicate-functionalized polycaprolactone scaffold, Regen Biomater 8 (6) (2021), rbab061.

[14] V. Fitzpatrick, Z. Martin-Moldes, A. Deck, R. Torres-Sanchez, A. Valat, D. Cairns, C. Li, D.L. Kaplan, Functionalized 3D-printed silk-hydroxyapatite scaffolds for enhanced bone regeneration with innervation and vascularization, Biomaterials 276 (2021), 120995.

[15] T.U. Wani, R.S. Khan, A.H. Rather, M.A. Beigh, F.A. Sheikh, Local dual delivery therapeutic strategies: using biomaterials for advanced bone tissue regeneration, J. Contr. Release 339 (2021) 143–155.

[16] X. Chen, B. Tan, Z. Bao, S. Wang, R. Tang, Z. Wang, G. Chen, S. Chen, W.W. Lu, D. Yang, S. Peng, Enhanced bone regeneration via spatiotemporal and controlled delivery of a genetically engineered BMP-2 in a composite Hydrogel, Biomaterials 277 (2021), 121117.

[17] D. Cao, Z. Xu, Y. Chen, Q. Ke, C. Zhang, Y. Guo, Ag-loaded MgSrFe-layered double hydroxide/chitosan composite scaffold with enhanced osteogenic and antibacterial property for bone engineering tissue, J. Biomed. Mater. Res. B Appl. Biomater. 106 (2) (2018) 863–873.

[18] Q. Li, D. Wang, J. Qiu, F. Peng, X. Liu, Regulating the local pH level of titanium via Mg-Fe layered double hydroxides films for enhanced osteogenesis, Biomater. Sci. 6 (5) (2018) 1227–1237.

[19] Y. Wang, S. Shen, T. Hu, G.R. Williams, Y. Bian, B. Feng, R. Liang, X. Weng, Layered double hydroxide modified bone cement promoting osseointegration via multiple osteogenic signal pathways, ACS Nano 15 (6) (2021) 9732–9745.

[20] M. Chu, Z. Sun, Z. Fan, D. Yu, Y. Mao, Y. Guo, Bi-directional regulation functions of lanthanum-substituted layered double hydroxide nanohybrid scaffolds via activating osteogenesis and inhibiting osteoclastogenesis for osteoporotic bone regeneration, Theranostics 11 (14) (2021) 6717–6734.

[21] Y. Wang, X. Mei, Y. Bian, T. Hu, X. Weng, R. Liang, M. Wei, Magnesium-based layered double hydroxide nanosheets: a new bone repair material with unprecedented osteogenic differentiation performance, Nanoscale 12 (37) (2020) 19075–19082.

[22] B. Dai, X. Li, J. Xu, Y. Zhu, L. Huang, W. Tong, H. Yao, D.H. Chow, L. Qin, Synergistic effects of magnesium ions and simvastatin on attenuation of high-fat diet-induced bone loss, Bioact. Mater. 6 (8) (2021) 2511–2522.

[23] Z. Zhai, X. Qu, H. Li, K. Yang, P. Wan, L. Tan, Z. Ouyang, X. Liu, B. Tian, F. Xiao, W. Wang, C. Jiang, T. Tang, Q. Fan, A. Qin, K. Dai, The effect of metallic magnesium degradation products on osteoclast-induced osteolysis and attenuation of NF-kappaB and NFATc1 signaling, Biomaterials 35 (24) (2014) 6299–6310.

[24] Z. Zhao, G. Li, H. Ruan, K. Chen, Z. Cai, G. Lu, R. Li, L. Deng, M. Cai, W. Cui, Capturing magnesium ions via microfluidic hydrogel microspheres for promoting cancellous bone regeneration, ACS Nano 3 (2021), 1c02147.

[25] Z. Wang, X. Wang, J. Pei, Y. Tian, J. Zhang, C. Jiang, J. Huang, Z. Pang, Y. Cao, X. Wang, S. An, X. Wang, H. Huang, G. Yuan, Z. Yan, Degradation and osteogenic induction of a SrHPO4-coated Mg-Nd-Zn-Zr alloy intramedullary nail in a rat femoral shaft fracture model, Biomaterials 247 (2020), 119962.

[26] H.M. Wong, K.W. Yeung, K.O. Lam, V. Tam, P.K. Chu, K.D. Luk, K.M. Cheung, A biodegradable polymer-based coating to control the performance of magnesium alloy orthopaedic implants, Biomaterials 31 (8) (2010) 2084–2096.

[27] Y. Li, C. Wen, D. Mushahary, R. Sravanthi, N. Harishankar, G. Pande, P. Hodgson, Mg-Zr-Sr alloys as biodegradable implant materials, Acta Biomater. 8 (8) (2012) 3177–3188.

[28] H. Kotani, H. Kawaguchi, T. Shimoaka, M. Iwasaka, S. Ueno, H. Ozawa, K. Nakamura, K. Hoshi, Strong static magnetic field stimulates bone formation to a definite orientation in vitro and in vivo, J. Bone Miner. Res. 17 (10) (2002) 1814–1821.

[29] Y. Xia, J. Sun, L. Zhao, F. Zhang, X.J. Liang, Y. Guo, M.D. Weir, M.A. Reynolds, N. Gu, H.H.K. Xu, Magnetic field and nano-scaffolds with stem cells to enhance bone regeneration, Biomaterials 183 (2018) 151–170.

[30] Y. Tang, Q. Wang, Q. Ke, C. Zhang, J. Guan, Y. Guo, Mineralization of ytterbium-doped hydroxyapatite nanorod arrays in magnetic chitosan scaffolds improves osteogenic and angiogenic abilities for bone defect healing, Chem. Eng. J. 387 (2020), 124166.

[31] W.Y.C. Shuai, C. He, S. Peng, C. Gao, Y. Yang, F. Qi, P. Feng, A magnetic micro-environment in scaffolds for stimulating bone regeneration, Mater. Des. 185 (2020) 108275.

[32] Y. Zhang, J. Li, P. Habibovic, Magnetically responsive nanofibrous ceramic scaffolds for on-demand motion and drug delivery, Bioact. Mater. 15 (2022) 372–381.

[33] Q. Wang, Y. Tang, Q. Ke, W. Yin, C. Zhang, Y. Guo, J. Guan, Magnetic lanthanum-doped hydroxyapatite/chitosan scaffolds with endogenous stem cell-recruiting and immunomodulatory properties for bone regeneration, J. Mater. Chem. B 8 (24) (2020) 5280–5292.

[34] Y. Huang, X. Shen, H. Qiao, H. Yang, X. Zhang, Y. Liu, H. Yang, Biofunctional Sr- and Si-loaded titania nanotube coating of Ti surfaces by anodization-hydrothermal process, Int. J. Nanomed. 13 (2018) 633–640.

[35] I. Ullah, W. Zhang, L. Yang, M.W. Ullah, O.M. Atta, S. Khan, B. Wu, T. Wu, X. Zhang, Impact of structural features of Sr/Fe co-doped HAp on the osteoblast proliferation and osteogenic differentiation for its application as a bone substitute, Mater Sci Eng C Mater Biol Appl 110 (2020), 110633.

[36] L. Yang, I. Ullah, K. Yu, W. Zhang, J. Zhou, T. Sun, L. Shi, S. Yao, K. Chen, X. Zhang, X. Guo, Bioactive Sr(2+)/Fe(3+)co-substituted hydroxyapatite in cryogenically 3D printed porous scaffolds for bone tissue engineering, Biofabrication 13 (3) (2021).

[37] N.H. Lee, M.S. Kang, T.H. Kim, D.S. Yoon, N. Mandakhbayar, S.B. Jo, H.S. Kim, J.C. Knowles, J.H. Lee, H.W. Kim, Dual actions of osteoclastic-inhibition and osteogenic-stimulation through strontium-releasing bioactive nanoscale cement imply biomaterial-enabled osteoporosis therapy, Biomaterials 276 (2021), 121025.

[38] S. Peng, X.S. Liu, G. Zhou, Z. Li, K.D. Luk, X.E. Guo, W.W. Lu, Osteoprotegerin deficiency attenuates strontium-mediated inhibition of osteoclastogenesis and bone resorption, J. Bone Miner. Res. 26 (6) (2011) 1272–1282.

[39] H. Wang, Y. Ma, J. Li, C. Zhou, A. Xu, Y. Xu, F. He, Modulating autophagy by strontium-doped micro/nano rough titanium surface for promotion of osteogenesis and inhibition of osteoclastogenesis, Colloids Surf. B Biointerfaces 210 (2022), 112246.

[40] H. Ye, J. Zhu, D. Deng, S. Jin, J. Li, Y. Man, Enhanced osteogenesis and angiogenesis by PCL/chitosan/Sr-doped calcium phosphate electrospun nanocomposite membrane for guided bone regeneration, J. Biomater. Sci. Polym. Ed. 30 (16) (2019) 1505–1522.

[41] S.K. Boda, G. Thrivikraman, B. Panigrahy, D.D. Sarma, B. Basu, Competing roles of substrate composition, microstructure, and sustained strontium release in directing osteogenic differentiation of hMSCs, ACS Appl. Mater. Interfaces 9 (23) (2017) 19389–19408.

[42] Y. Sun, Y. Li, Y. Zhang, T. Wang, K. Lin, J. Liu, A polydopamine-assisted strontium-substituted apatite coating for titanium promotes osteogenesis and angiogenesis via FAK/MAPK and PI3K/AKT signaling pathways, Mater Sci Eng C Mater Biol Appl 131 (2021), 112482.

[43] L. Liu, F. Yu, L. Li, L. Zhou, T. Zhou, Y. Xu, K. Lin, B. Fang, L. Xia, Bone marrow stromal cells stimulated by strontium-substituted calcium silicate ceramics: release of exosomal miR-146a regulates osteogenesis and angiogenesis, Acta Biomater. 119 (2021) 444–457.

[44] T. Li, H. He, Z. Yang, J. Wang, Y. Zhang, G. He, J. Huang, D. Song, J. Ni, X. Zhou, J. Zhu, M. Ding, Strontium-doped gelatin scaffolds promote M2 macrophage switch and angiogenesis through modulating the polarization of neutrophils, Biomater. Sci. 9 (8) (2021) 2931–2946.

[45] R. Schmidt, A. Gebert, M. Schumacher, V. Hoffmann, A. Voss, S. Pilz, M. Uhlemann, A. Lode, M. Gelinsky, Electrodeposition of Sr-substituted hydroxyapatite on low modulus beta-type Ti-45Nb and effect on in vitro Sr release and cell response, Mater Sci Eng C Mater Biol Appl 108 (2020), 110425.

[46] S. Zhu, X. Hu, Y. Tao, Z. Ping, L. Wang, J. Shi, X. Wu, W. Zhang, H. Yang, Z. Nie, Y. Xu, Z. Wang, D. Geng, Strontium inhibits titanium particle-induced osteoclast activation and chronic inflammation via suppression of NF-kappaB pathway, Sci. Rep. 6 (2016), 36251.

[47] E. Buache, F. Velard, E. Bauden, C. Guillaume, E. Jallot, J.M. Nedelec, D. Laurent-Maquin, P. Laquerriere, Effect of strontium-substituted biphasic calcium phosphate on inflammatory mediators production by human monocytes, Acta Biomater. 8 (8) (2012) 3113–3119.

[48] H. Bai, F. Walsh, B. Gludovatz, B. Delattre, C. Huang, Y. Chen, A.P. Tomsia, R.O. Ritchie, Bioinspired hydroxyapatite/poly(methyl methacrylate) composite with a nacre-mimetic architecture by a bidirectional freezing method, Adv. Mater. 28 (1) (2016) 50–56.
[49] R.L. Yang, Y.J. Zhu, F.F. Chen, D.D. Qin, Z.C. Xiong, Bioinspired macroscopic ribbon fibers with a nacre-mimetic architecture based on highly ordered alignment of ultralong hydroxyapatite nanowires, ACS Nano 12 (12) (2018) 12284–12295.
[50] Y.W. Ge, X.L. Liu, D.G. Yu, Z.A. Zhu, Q.F. Ke, Y.Q. Mao, Y.P. Guo, J.W. Zhang, Graphene-modified CePO4 nanorods effectively treat breast cancer-induced bone metastases and regulate macrophage polarization to improve osteo-inductive ability, J. Nanobiotechnol. 19 (1) (2021) 11.
[51] Y.W. Ge, J.W. Lu, Z.Y. Sun, Z.Q. Liu, J. Zhou, Q.F. Ke, Y.Q. Mao, Y.P. Guo, Z.A. Zhu, Ursolic acid loaded-mesoporous bioglass/chitosan porous scaffolds as drug delivery system for bone regeneration, Nanomedicine 18 (2019) 336–346.
[52] L.Z.Y.L.S.X.R.L.X.Z.F. Zhang, Intercalation of perfluorobutane sulfonate into layered double hydroxides Appl, Clay Sci. 48 (2010) 5.
[53] J.M. Coulson, B.W. Hughes, Dose-response relationships in aluminium toxicity in humans, Clin. Toxicol. 60 (4) (2022) 415–428.
[54] J. Zhang, Y. Li, C. Liu, J. Sun, Y. Zhao, Effects of Fe3+ and Fe2+ on proliferation, differentiation and mineralization function of primary osteoblasts in vitro, Chin. J. Inorg. Chem. 25 (2009) 6.
[55] Y. Kong, X. Hu, Y. Zhong, K. Xu, B. Wu, J. Zheng, Magnesium-enriched microenvironment promotes odontogenic differentiation in human dental pulp stem cells by activating ERK/BMP2/Smads signaling, Stem Cell Res. Ther. 10 (1) (2019) 378.
[56] S. Kokabu, J. Nojima, K. Kanomata, S. Ohte, T. Yoda, T. Fukuda, T. Katagiri, Protein phosphatase magnesium-dependent 1A-mediated inhibition of BMP signaling is independent of Smad dephosphorylation, J. Bone Miner. Res. 25 (3) (2010) 653–660.
[57] W. Zhang, Y. Tian, H. He, R. Chen, Y. Ma, H. Guo, Y. Yuan, C. Liu, Strontium attenuates rhBMP-2-induced osteogenic differentiation via formation of Sr-rhBMP-2 complex and suppression of Smad-dependent signaling pathway, Acta Biomater. 33 (2016) 290–300.
[58] S.S. Singh, A. Roy, B. Lee, P.N. Kumta, Study of hMSC proliferation and differentiation on Mg and Mg-Sr containing biphasic beta-tricalcium phosphate and amorphous calcium phosphate ceramics, Mater Sci Eng C Mater Biol Appl 64 (2016) 219–228.
[59] C. Zhao, P. Zhang, J. Zhou, S. Qi, Y. Yamauchi, R. Shi, R. Fang, Y. Ishida, S. Wang, A.P. Tomsia, M. Liu, L. Jiang, Layered nanocomposites by shear-flow-induced alignment of nanosheets, Nature 580 (7802) (2020) 210–215.
[60] G. Xin, W. Zhu, Y. Deng, J. Cheng, L.T. Zhang, A.J. Chung, S. De, J. Lian, Microfluidics-enabled orientation and microstructure control of macroscopic graphene fibres, Nat. Nanotechnol. 14 (2) (2019) 168–175.
[61] S. Deville, E. Saiz, R.K. Nalla, A.P. Tomsia, Freezing as a path to build complex composites, Science 311 (5760) (2006) 515–518.
[62] J. Lee, H. Byun, S.K. Madhurakkat Perikamana, S. Lee, H. Shin, Current advances in immunomodulatory biomaterials for bone regeneration, Adv Healthc Mater 8 (4) (2019), e1801106.
[63] X. Liu, M. Chen, J. Luo, H. Zhao, X. Zhou, Q. Gu, H. Yang, X. Zhu, W. Cui, Q. Shi, Immunopolarization-regulated 3D printed-electrospun fibrous scaffolds for bone regeneration, Biomaterials 276 (2021), 121037.
[64] D. Yang, J. Xiao, B. Wang, L. Li, X. Kong, J. Liao, The immune reaction and degradation fate of scaffold in cartilage/bone tissue engineering, Mater Sci Eng C Mater Biol Appl 104 (2019), 109927.
[65] Y. Sheng, J. Yang, X. Zhao, H. Liu, S. Cui, L. Chen, R. Zeng, X. Wang, C.H. Huang, W. Li, Development and in vitro biodegradation of biomimetic zwitterionic phosphorylcholine chitosan coating on Zn1Mg alloy, ACS Appl. Mater. Interfaces 12 (49) (2020) 54445–54458.
[66] M.S. Cortizo, M.S. Molinuevo, A.M. Cortizo, Biocompatibility and biodegradation of polyester and polyfumarate based-scaffolds for bone tissue engineering, J Tissue Eng Regen Med 2 (1) (2008) 33–42.